The comparative hydrodynamics of rapid rotation by predatory appendages

M. J. McHenry[1], P. S. L. Anderson[2,*,‡], S. Van Wassenbergh[3,4,‡], D. G. Matthews[5], A. P. Summers[6] and S. N. Patek[2,§]

ABSTRACT

Countless aquatic animals rotate appendages through the water, yet fluid forces are typically modeled with translational motion. To elucidate the hydrodynamics of rotation, we analyzed the raptorial appendages of mantis shrimp (Stomatopoda) using a combination of flume experiments, mathematical modeling and phylogenetic comparative analyses. We found that computationally efficient blade-element models offered an accurate first-order approximation of drag, when compared with a more elaborate computational fluid-dynamic model. Taking advantage of this efficiency, we compared the hydrodynamics of the raptorial appendage in different species, including a newly measured spearing species, *Coronis scolopendra*. The ultrafast appendages of a smasher species (*Odontodactylus scyllarus*) were an order of magnitude smaller, yet experienced values of drag-induced torque similar to those of a spearing species (*Lysiosquillina maculata*). The dactyl, a stabbing segment that can be opened at the distal end of the appendage, generated substantial additional drag in the smasher, but not in the spearer, which uses the segment to capture evasive prey. Phylogenetic comparative analyses revealed that larger mantis shrimp species strike more slowly, regardless of whether they smash or spear their prey. In summary, drag was minimally affected by shape, whereas size, speed and dactyl orientation dominated and differentiated the hydrodynamic forces across species and sizes. This study demonstrates the utility of simple mathematical modeling for comparative analyses and illustrates the multi-faceted consequences of drag during the evolutionary diversification of rotating appendages.

KEY WORDS: Drag, Feeding, Kinematics, Torque, Scaling, Phylogenetic comparative methods

INTRODUCTION

The diverse array of aquatic animals that rotate their appendages for locomotion and prey capture offers rich material for considering the role of hydrodynamics in morphological and kinematic diversification (Fish, 1984; Johansson and Lauder, 2004; Koehl, 1996; McHenry et al., 2003; Ngo and McHenry, 2014; Richards, 2010; Webb and Blake, 1985). Although the drag forces in terrestrial systems are often negligible, the aquatic appendages of dragonfly larvae, snapping shrimp and mantis shrimp, for example, necessarily incur substantial drag (Anker et al., 2006; McHenry et al., 2012; Tanaka and Hisada, 1980; Versluis et al., 2000). Therefore, relationships among the parameters that influence drag have the potential to inform interpretations of morphological diversity.

Shape, size and velocity influence how drag resists the motion of a body moving through water. Drag is generated by shear stress and pressure differences that the fluid generates along the body's surface. When the body is translated through the water, drag (F_d) is commonly modeled with the following equation:

$$F_d = \frac{1}{2} C_d \rho S v^2, \tag{1}$$

where ρ is the density of the fluid medium, S is a characteristic surface area of the object moving through the fluid, v is the linear velocity of the object relative to the fluid and C_d is the drag coefficient, a non-dimensional measure of shape. The drag coefficient is typically determined from drag measured by a force transducer for a body exposed to the uniform flow generated by a flume (e.g. Van Wassenbergh et al., 2015b). In contrast, a rotating body is exposed to flow that varies linearly along its length. A blade-element model of drag may account for this position dependency as the sum of elements along the appendage's length (Blake, 1979). For each instant in the rotation of an appendage, this sum may be formulated from measurements of the dimensions of each element, probable values for its drag coefficient, and its position-dependent velocity (McHenry et al., 2003). This approach treats all elements as independent force-generating units and thereby neglects factors such as span-wise flow and the high shear stress that may be generated at the distal end (e.g. Dickinson et al., 1999; Lentink et al., 2009). The relative simplicity of the blade-element approach yields a method for calculating drag that is computationally efficient and therefore amenable to comparative analysis (Richards, 2010; Walker, 2004). However, it is unclear whether the simplifying assumptions of a blade-element approach are violated for any particular rotating appendage. Therefore, the present study compared the predictions by blade-element modeling against both experimental approaches and more elaborate computational analyses.

To fully incorporate the effects of rotation on hydrodynamics, many studies have employed computational fluid dynamics (CFD) (e.g. Jiang and Kiørboe, 2011; Li et al., 2012; Liu et al., 1996; Van Wassenbergh et al., 2015a). CFD analyses can consider the fluid forces generated by complex geometries with fully resolved volumetric flow fields. However, the investment in the development and computational resources to perform CFD simulations are sufficiently intensive that they typically preclude

[1]Department of Ecology & Evolutionary Biology, 321 Steinhaus Hall, University of California, Irvine, Irvine, CA 92697-2525, USA. [2]Department of Biology, Duke University, Durham, NC 27708, USA. [3]Department of Biology, Universiteit Antwerpen, Universiteitsplein 1, Antwerpen 2610, Belgium. [4]Département d'Ecologie et de Gestion de la Biodiversité, UMR 7179 CNRS/MNHN, 57 rue Cuvier, Case Postale 55, Paris Cedex 05 75231, France. [5]Department of Biology, University of Massachusetts Amherst, Amherst, MA 01002, USA. [6]Friday Harbor Laboratories, University of Washington, 620 University Rd., Friday Harbor, WA 98250, USA.
*Present address: Department of Animal Biology, University of Illinois, Urbana-Champaign, Urbana, IL 61801, USA.
‡These authors contributed equally to this work

§Author for correspondence (snp2@duke.edu)

S.N.P., 0000-0001-9738-882X

List of symbols and abbreviations

c	chord length; linear dimension in direction of flow (m)
C_d	drag coefficient (dimensionless)
CFD	computational fluid dynamics
E_d	energy lost due to drag (J)
F_d	drag (N)
h	width; linear dimension perpendicular to flow (m)
i	element number
k	shape coefficient (dimensionless)
l	thickness; linear dimension along the longitudinal axis of the structure (m)
L	characteristic length (m)
micro-CT	micro-computed tomography
MSE	mean-squared error
n	number of elements
PGLS	phylogenetic generalized least squares
r	distance to pivot point (m)
Re	Reynolds number (dimensionless)
S	surface area (m^2)
t	time (s)
T	strike duration (s)
T_d	drag-torque index (dimensionless)
U	velocity of fluid in flume (m s^{-1})
v	velocity of object relative to fluid (m s^{-1})
γ	angle of dactyl/propodus rotation (rad)
μ	dynamic viscosity (Pa s)
ρ	density (kg m^{-3})
τ	drag torque (N)

large-scale comparative, evolutionary analyses that incorporate detailed morphological variation. An analysis of rapidly rotating pipefish snouts found that CFD models agreed with the predictions of a more simple blade-element model, where drag was treated as the sum of independent structural elements with linear flow assumed (Van Wassenbergh and Aerts, 2008). Similarly, an analysis of a hovering fruit fly also yielded convergent results between blade-element and CFD models (Walker, 2002). In contrast, in the context of the more complex aerodynamics of flapping flight, a modified CFD analysis performed better than a blade-element approach (Nakata et al., 2015).

Mantis shrimp (Stomatopoda) offer an intriguing system in which to examine the effects of shape, size and velocity on drag forces (Fig. 1). 'Smasher' mantis shrimp evolved from 'spearers' (Porter et al., 2010) and, during this transition, the dactyl-open evasive prey capture motion characteristic of spearers switched to a primarily closed-dactyl, hammering motion directed at hard-shelled prey (Patek, 2015). Along with this shift in the orientation and target of the raptorial strike, smashers dramatically increased in speeds and accelerations (Table 1) (Cox et al., 2014; deVries et al., 2012; Kagaya and Patek, 2016), evolved enhanced elastic energy storage capabilities (Patek et al., 2013; Rosario and Patek, 2015), yet also experienced a substantial decrease in range of body size and appendage size compared with their ancestral spearers (Anderson et al., 2014; Blanco and Patek, 2014). Thus, the evolutionary shift to smashing encapsulates the major axes of drag: shape, speed and size.

The goal of the present study was to analyze the hydrodynamic consequences of kinematic and morphological variation in the fast rotational motion of the mantis shrimp raptorial appendage. We evaluated the methods of drag measurement, blade-element modeling and CFD to quantify drag on this rapidly rotating structure. In addition, we performed a new kinematic analysis of a spearing mantis shrimp, *Coronis scolopendra*, and conducted phylogenetic comparative analyses of the relationships among drag-related parameters across mantis shrimp. We considered the torque generated by drag (henceforth referred to as 'drag-torque') and the propensity of an appendage to generate this torque, which was measured with the drag-torque index (McHenry et al., 2012). These approaches allowed us to address three guiding questions: (1) how does the balance of evolutionary variation in kinematics, shape and size influence variation in drag across stomatopods; (2) given the wide range of high Reynolds numbers (*Re*) for this system (Table 1), can we make simplifying assumptions about drag calculations, in the context of the added complexities of rotational, rather than translational, motion; and (3) given the results of the comparative analyses and fluid dynamic methodological comparisons, which aspects of mantis shrimp fluid dynamics are most relevant to evolutionary diversification and should be the primary focus of future fluid dynamic analyses in mantis shrimp?
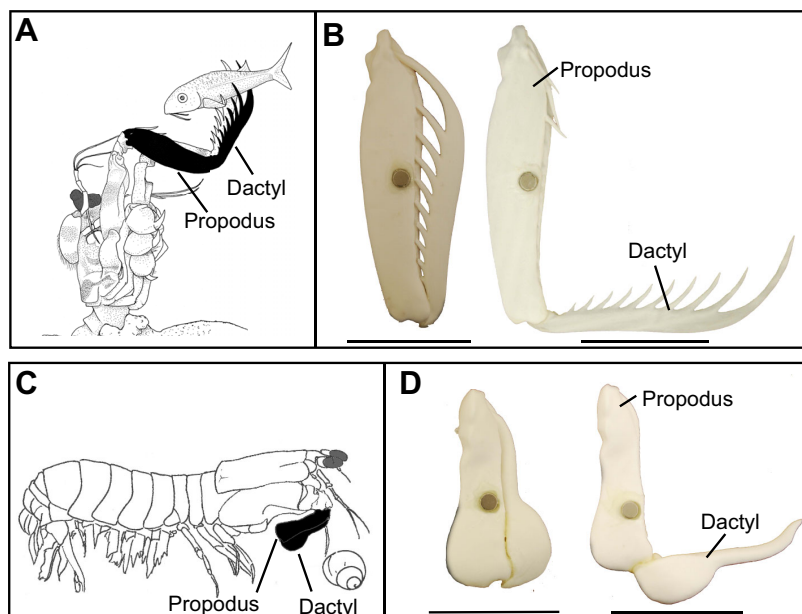

Fig. 1. Stomatopod appendages vary in shape, size and strike kinematics, depending on their predatory strategies. (A) *Lysiosquillina maculata* ambushes evasive prey using spines on the dactyl and propodus. (B) In spearers, the dactyl and propodus form a rotating unit during a strike, most often with the dactyl open and extended toward the prey. These physical models, scaled up to match the Reynolds number of an actual strike, were positioned in the flume with the dactyl either closed against the propodus (left) or opened away from the propodus (right). (C) *Gonodactylus smithii* smashes hard-shelled prey using a bulbous hammer at the base of the dactyl. (D) Hammering occurs with the dactyl folded against the propodus (left), but these animals can stab with the dactyl in the open position (right). The physical models (B,D) were placed in the dactyl-open and dactyl-closed orientations for the flume tests. Scale bars are 10 mm. Drawings in A and C are adapted from deVries et al. (2012) and Caldwell and Dingle (1976), respectively.

Table 1. Raptorial appendage size and kinematics across six mantis shrimp species

	Neogonodactylus bredini	*Odontodactylus scyllarus*	*Gonodactylus smithii*	*Lysiosquillina maculata*	*Coronis scolopendra*	*Alachosquilla vicina*
Raptorial appendage type	Smasher	Smasher	Smasher	Spearer	Spearer	Spearer
Sample size: no. individuals (strikes per individual)	5 (11–24)	6 (7–11)	5 (10)	5 (3–7)	7 (5–10)	4–5 (1–12)
Propodus length (cm)	0.78±0.18 (0.58–1.00)	2.46±0.33 (2.02–2.95)	0.73±0.18 (0.54–0.96)	3.48±0.79 (2.59–4.71)	0.76±0.09 (0.56–0.83)	0.42±0.03 (0.38–0.46)
Striking body length (cm)	0.87±0.16 (0.74–1.07)	2.65±0.36 (2.22–3.22)	0.82±0.25 (0.59–1.12)	3.68±0.75 (2.79–4.78)	0.84±0.10 (0.63–0.92)	0.48±0.04 (0.43–0.52)
Speed (m s⁻¹)	11.3±4.9 (2.8–21.6)	14.0±1.8 (4.5–25.4)	20.2±4.1 (7.2–30.6)	2.3±0.5 (1.2–4.5)	2.1±0.6 (0.7–3.6)	5.7±0.9 (4.0–8.5)
Angular velocity (rad s⁻¹)	1585±755 (379–3298)	605±51 (163–987)	2821±682 (1175–4976)	64.7±13.9 (25.7–124.3)	296±149 (93–690)	1610±342 (1003–2694)
Linear acceleration (m s⁻²)	3.6×10⁴±2.6×10⁴ (0.2×10⁴–9.5×10⁴)	5.6×10⁴±7300 (2.0×10⁴–1.0×10⁵)	7.8×10⁴±2.4×10⁴ (2.0×10⁴–2.5×10⁵)	0.29±0.14 (0.04–1.80)	2600±1200 (300–1.1×10⁴)	9100±3300 (1300–1.6×10⁴)
Angular acceleration (rad s⁻²)	5.8×10⁶±4.4×10⁶ (2.4×10⁵–1.8×10⁷)	9.4×10⁵±9.6×10⁴ (2.1×10⁵–2.0×10⁶)	1.1×10⁷±5.3×10⁶ (3.2×10⁶–3.6×10⁷)	8.3±4.4 (1.1–53.0)	3.9×10⁵±2.9×10⁵ (3.6×10⁴–1.8×10⁶)	2.6×10⁶±1.0×10⁶ (3.3×10⁵–5.1×10⁶)
Duration (10⁻³ s)	–	2.7±0.5 (1.6–5.2)	0.84±0.20 (0.28–2.00)	34.7±9.9 (20.0–70.0)	6.7±2.2 (2.3–13.1)	3.3±0.4 (1.9–4.5)
Time to maximum speed (10⁻³ s)	1.14±0.56 (0.54–2.89)	–	0.72±0.17 (0.27–1.43)	15.5±5.4 (10.0–40.0)	2.7±1.0 (0.2–6.1)	1.1±0.2 (0.7–1.5)[1]
Imaging rate (frames s⁻¹)	30,000	5000	30,000	3000	10,000–15,000	10,000
Reynolds number	9.3×10⁴	3.5×10⁵	1.6×10⁵	8.0×10⁴	1.7×10⁴	2.6×10⁴
Source	Kagaya and Patek, 2016	Patek et al., 2004	Cox et al., 2014 (reanalyzed)	deVries et al., 2012 (reanalyzed)	Present study	deVries et al., 2012

Data from the present study and previous studies were compiled to examine the effects of scaling and kinematics on strike energetics. Several datasets were reanalyzed to make the analyses consistent across the datasets. Reynolds numbers are calculated based on the instantaneous peak speed and striking body length, both averaged for each species.

MATERIALS AND METHODS

Strike kinematics of *Coronis scolopendra*

We supplemented previously published kinematics of very small and larger spearers through high-speed videos of a medium-sized spearer, *Coronis scolopendra* Latreille 1828 (Crustacea: Stomatopoda: Lysiosquilloidea: Nannosquillidae). Individuals were collected in Florida (Florida Division of Marine Fisheries Management, license no. SAL-13-1278-SRP) and kept in aquaria (24–28°C, 34–36 ppt salinity), where the animals formed their own burrows (sugar-sized Oolite, Aragonite, CaribSea, White City, FL, USA). They struck live brine shrimp introduced by pipette or forceps and were filmed using a digital high-speed imaging system (10,000–15,000 frames s⁻¹, 1/10,000–1/15,000 shutter, 512×512–512×256 pixels, APX-RS, Photron Inc., San Diego, CA, USA). A ruler was placed in the plane of the striking animal to calibrate each series of videos.

Five points were tracked manually in each image sequence of a raptorial appendage strike (Fig. 2). Tracking began when the carpus rotation started, and ended when the appendage made contact with the prey or feeding device (MATLAB v. R2011a, The MathWorks, Natick, MA, USA). The five points included a central point on the merus as well as points on the distal ends of the merus, carpus, propodus and dactyl (Fig. 2). The percent error in each measured displacement averaged 9.2±3.5% (range 3.5–16.5%), assessed by 10 repeated measures of a representative strike.

Kinematics were calculated from the coordinate measurements (MATLAB v. R2013b, The MathWorks). Rates of change were calculated from the first and second derivatives of a least-squares fit to a 10th-order polynomial determined to positional data (Cox et al., 2014; deVries et al., 2012). If maximum speed occurred at the beginning or end of the digitized portion of the strike, then the strike was eliminated from the dataset, because the true peak speed could have occurred outside the digitized segment of the strike. Using linear models, we tested whether kinematics were correlated with body size
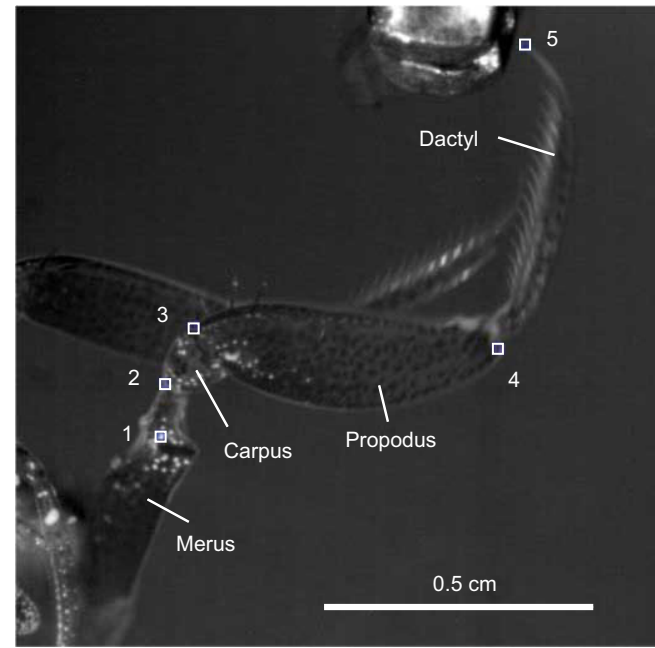

Fig. 2. Five points were tracked on each *Coronis scolopendra* individual's raptorial appendage during predatory strikes. The points correspond to: (1) central merus, (2) distal end of the merus, (3) distal end of the carpus, (4) distal end of the propodus and (5) distal end of the dactyl. This animal's raptorial appendage is shown in lateral view with distal toward the right of the page.

(R v. 3.0.2, R Foundation for Statistical Computing, Vienna, Austria) using propodus length as a proxy for body size (Claverie et al., 2011; deVries et al., 2012; Patek and Caldwell, 2005).

Strike kinematics across species

We used previously published and *C. scolopendra* strike kinematics to determine scaling relationships. We incorporated kinematics from *Lysiosquillina maculata* and *Alachosquilla vicina* (deVries et al., 2012), *Gonodactylus smithii* (Cox et al., 2014; Patek et al., 2007) and *Neogonodactylus bredini* (Kagaya and Patek, 2016) in a form consistent with present measurements. We measured the propodus length (length of the propodus between the propodus–dactyl joint to the proximal-most point visible on the propodus) and the striking body length (length from the propodus–dactyl joint to the insertion point of the lateral extensor muscle on the dorsal surface of the carpus) from archived digital images (Fig. 3).

We performed phylogenetic generalized least squares (PGLS) regression on logged species averages against logged average striking body length to examine the relationship between size and kinematics across species. Maximum kinematic values for each individual were
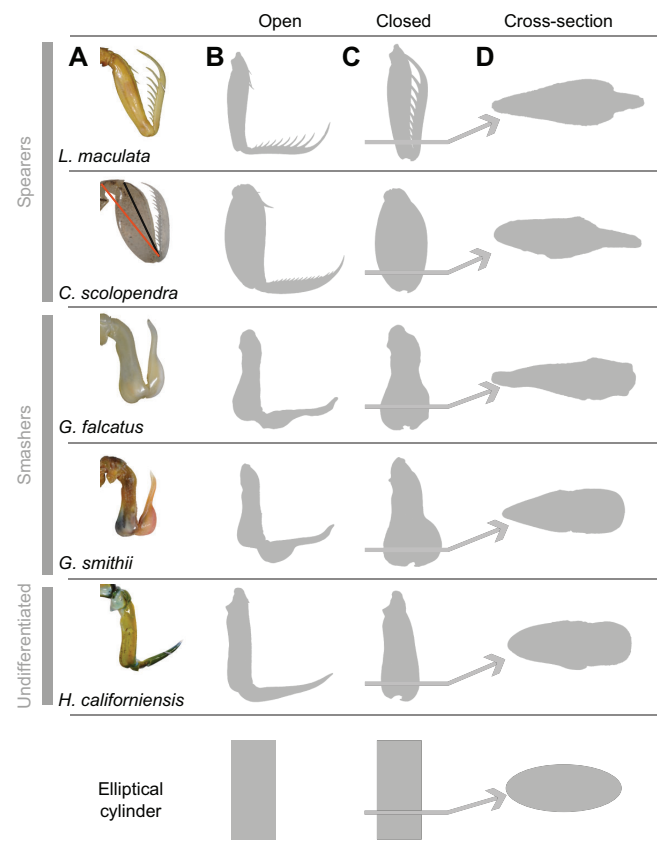

Fig. 3. Drag was measured using 10 appendage models from five taxa, with the dactyls oriented in both open and closed positions. (A) Taxa measured were: *Lysiosquillina maculata*, *Coronis scolopendra*, *Gonodactylaceus falcatus*, *Gonodactylus smithii* and *Hemisquilla californiensis*. (B) Open position; (C) closed position. (D) The effect of cross-sectional shape was assessed through direct measurements on the appendages with the dactyl closed and through comparison with an elliptical cylinder. Propodus length (black line) and striking body length (orange line) are indicated on the photo of *C. scolopendra*. Appendage models were scaled up from their actual size to maintain a constant Reynolds number in the flume experiments. Silhouettes and images are not to scale.

used to calculate the average maximum value for each species. We incorporated a pruned and time-calibrated molecular phylogenetic tree based on nucleotide sequence data (Porter et al., 2010) with hard-bound calibration points from fossil data to establish time calibrations (Claverie and Patek, 2013). PGLS analyses were performed in the R package 'caper' (https://cran.r-project.org/web/packages/caper/index.html), with delta and kappa fixed at unity and lambda estimated using maximum-likelihood methods, which allows the model to deviate from a strict Brownian motion.

We compared three species to explore the effects of strike kinematics on fluid forces. *Gonodactylus smithii* was employed as a representative smasher, *L. maculata* represented large spearers and *A. vicina* served as a characteristic small spearer (Fig. 3). We applied a sensitivity analysis that examined the effects of kinematics on the maximum torque and energetic expense generated by drag (described below). The striking motion, defined as the angle of the propodus–dactyl unit during a strike with respect to time, approximated a sigmoidal curve for all species. The species primarily differed in terms of strike duration and angular excursion of the appendage. We found that the excursion, γ_d (in radians), was correlated with the strike duration (in seconds), T, as specified by the following equation:

$$\gamma_d = 35.7T + 1.1. \tag{2}$$

Therefore, much of the variation in strike kinematics across species may be explained by differences in strike duration.

We approximated the strike kinematics of each species using one average strike from *L. maculata* that exhibited the characteristic sigmoidal pattern that we found in all species (Fig. S1). After normalizing for the strike duration and maximum excursion, we used a non-linear least-squares fit to characterize this strike with the following fifth-order polynomial:

$$\bar{\gamma} = -1.45\,\bar{t}^5 + 0.72\,\bar{t}^4 + 3.48\,\bar{t}^3 - 2.89\,\bar{t}^2 + 1.13\,\bar{t}, \tag{3}$$

where $\bar{\gamma}$ and $\bar{t}$ are the respective values of normalized angular position and time. This pattern was used to vary the kinematics across species by multiplying normalized time values by the strike duration and the normalized angular position by the corresponding angular excursion (using Eqn 2). This approximation was validated by comparing the performance for kinematics of Eqn 3 against the measured kinematics of equal duration using a Kolmogorov–Smirnov goodness-of-fit test for *G. smithii* (drag energy: $P=0.64$; maximum torque: $P=0.47$; $N=47$), *C. scolopendra* (drag energy: $P=0.36$; maximum torque: $P=0.68$; $N=50$) and *L. maculata* (drag energy: $P=0.16$; maximum torque: $P=0.08$; $N=58$). Calculations of the mean-squared error (MSE) for the fit (*G. smithii*: MSE=0.039 rad^2; *C. scolopendra*: MSE=0.005 rad^2; *L. maculata*: MSE=0.262 rad^2) indicated that the spearer, *L. maculata*, exhibited substantial variation not represented by Eqn 3.

Drag measurements on physical models

Our experimental consideration of raptorial appendage fluid dynamics was based on drag measurements from physical models. These models were created with 3D prints that were dynamically scaled to approximate Re of striking appendages (Fig. 3, Table S1). Re is given by the following equation:

$$Re = \frac{\rho U L}{\mu}, \tag{4}$$

where U is the velocity of flow, L is a characteristic length, and ρ and μ are, respectively, the density and dynamic viscosity of

water. The characteristic length is commonly selected as a dimension in the direction of flow, whereas we used the propodus length because of the irregularity of the cross-sectional shape in the direction of flow. The 3D prints were enlarged to compensate for the slow flow speeds generated by the flume. Prints for two of the taxa did not have published kinematic data, so the scaling was based on speed from similar taxa. In particular, *Gonodactylaceus falcatus* models were assumed to have speed similar to *G. smithii*, and *Hemisquilla californiensis* were approximated by the speed of *L. maculata*. For the three relatively slow species (*H. californiensis*: undifferentiated; *L. maculata* and *C. scolopendra*: spearers), we were able to match and exceed the *Re* of measured strikes (Table S1). We used the smaller end of the size range for the smashers *G. smithii* and *G. falcatus* to correctly match their *Re* while accommodating the limits to the size of the 3D printer (Z-Corp 310, 3D Systems, Rock Hill, SC, USA) and the top speed of the flume (1 m s^{-1}, model 2436, Rolling Hills Research, El Segundo, CA, USA) (Table S1).

The 3D printed models were based on scans of the dactyl and propodus segments acquired from micro-computed tomography (micro-CT; Model HMXST225, X-Tek, Nikon Metrology NV, Leuven, Belgium). The carpus, which is proximal to the propodus, was excluded because of its modest contribution to the generation of drag (McHenry et al., 2012). The scans were performed for two smasher species (*G. smithii* and *G. falcatus*), two spearer species (*C. scolopendra* and *L. maculata*) and an undifferentiated species (*H. californiensis*) (Figs 1, 3). The individual dactyl and propodus segments were digitally separated (Mimics v13.0 for X64, Materialize, Belgium) and their wetted surfaces were identified and smoothed (Geomagic Studio 11, 64-bit edition, Geomagic, Cary, NC, USA). The resulting geometries were printed and then hardened with cyanoacrylate to create enlarged physical models of the dactyl and propodus that could be mounted with the dactyl in either an opened or closed position relative to the propodus (Fig. 1).

We measured the drag on the physical models over a range of flow. Each physical model was suspended in the working section of the flume with the long-axis of the propodus perpendicular and the dactyl opened toward oncoming flow (Fig. 4). The sting holding each model was positioned such that force was applied in the direction of flow velocity (Fig. 4) against a force sensor (DS2-4, Imada, Northbrook, IL, USA) for a 1-min recording (SW-1 Data Acquisition package, Imada). The drag generated by the sting was subtracted from each measurement.

Computational fluid dynamics

We tested a blade-element model of the hydrodynamics of a rotating structure with CFD. We animated the CFD model with the strike kinematics of the smasher, *G. smithii*, and approximated its geometry with a series of 19 frustum segments (virtual slices of the appendage) connecting 20 ellipses that match the cross-sectional shape along the length of the appendage (Fig. S2). This multi-frustum model was created in the CAD program GAMBIT v. 2.4.6 (ANSYS, Canonsburg, PA, USA) and then imported into ANSYS DesignModeler 14.5.7, where it was surrounded by a spherical flow domain with a radius of 0.05 m. The flow domain was meshed with 11 million tetrahedrals, with a density decreasing with distance away from the appendage (growth rate 1.1 per layer starting from a mesh element size of 20 µm, ANSYS Meshing 14.5.7). This density was sufficient, as suggested by a simulation with one-third of the number of tetrahedrals, which predicted the maximum hydrodynamic torque to differ by only 1.5%. The model was subjected to a constant acceleration of 4×10^6 rad s^{-2}, from standstill to 2800 rad s^{-1} in 0.70 ms, which corresponds closely to the values (2821 rad s^{-1} at 0.72 ms) for *G. smithii* (Table 1). Simulations solved the flow field for the full Navier–Stokes equations for unsteady laminar flow (ANSYS Fluent 14.5.7) with a fixed time-step (3.5 µs). Quartering the time-step size had a negligible effect on the calculated torque (<0.7% difference). In these simulations, the mesh of the entire flow domain was rotated at constant acceleration with respect to the fixed reference frame (DEFINE-ZONE-MOTION function in Fluent). The outer boundary of the spherical flow domain was defined as a pressure outlet with zero-gauge pressure and backflow perpendicular to the no-slip boundary of the appendage.

The torque generated by drag was determined by summing the torques due to viscous and pressure forces on each surface element of the multi-frustum model. This calculation was compared with the prediction for the same conditions by a blade-element model, as done previously (Van Wassenbergh et al., 2008). As detailed below, a blade-element model calculates the quasi-steady fluid forces as the sum of forces generated by virtual sections along the structure. In this implementation, the mantis shrimp appendage was divided into 19 segments and the torques generated by drag and added mass were calculated for each interval of time (eqns 2.6 to 2.15 in Van Wassenbergh et al., 2008).

We compared the drag generated by rotational motion with that generated by linear motion. This was achieved by CFD simulations with the multi-frustum model in steady, linear flow of 20 m s^{-1} with a cylindrical flow domain (0.3 m in length,
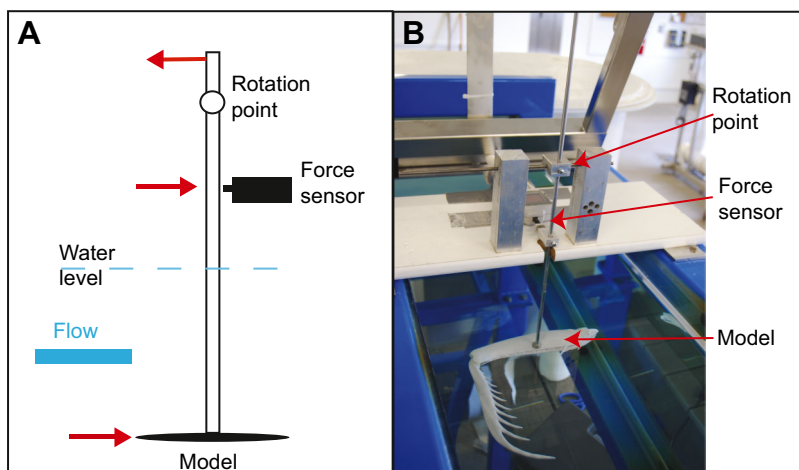

Fig. 4. Drag was measured experimentally using physical models placed in a flume. The vertical rod acted as a lever, which rotates around a beam suspended above the water. The model was affixed to the bottom of the rod. The water flow pushed on the model and rotated the rod. The rod made contact with the force gauge when rotated, thereby measuring the force produced by the flow. (A) Schematic of the experimental setup. (B) Labeled photograph of the experimental setup.

0.05 m in radius). The appendage was oriented perpendicular to the central axis of the cylinder. Pressure inlets and outlets at the ends of the cylinder induced flow along this axis toward the leading edge of the appendage. The walls of the cylinder were defined with a velocity equal to freestream flow (20 m s^{-1}) and the multi-frustum surface was defined with a no-slip condition. We used Menter's shear stress transport model in ANSYS Fluent (Menter, 1994) to resolve the flow patterns in the wake, which accurately calculates the steady-state drag of bluff bodies at similar Re (Goyens et al., 2015; Van Wassenbergh et al., 2015b). A mesh convergence analysis showed that the drag did not vary substantially when refining from 11 million to 16 million cells (+0.1%) (Fig. S3). We retained the latter density for our simulations (mesh size at the multi-frustum surface of 1.6 µm), which showed convergence after 2000 iterations. The drag coefficients of each individual frustum segment, as well as the overall drag on the model, were calculated from the solution.

To evaluate the influence of the drag coefficient (C_d) on the accuracy of the blade-element model, three versions of blade-element models were compared: (1) a model using C_d values from measurements of a range of long elliptical cylinders with different aspect ratios (see Eqn 5 below), (2) a model that used the C_d values calculated for each individual frustum segment of the steady-flow CFD simulation described above, and (3) a model that used the total drag force from the steady-flow CFD simulation. To focus on the effect of drag forces, differences in added-mass torque between the blade-element models and CFD at the instant of pure added mass resistance (the first time steps of the simulation when velocity is very low and drag is negligible) were cancelled out by adding a constant torque (8.54×10^{-5} N m or 19% of the CFD's added mass torque). This analysis allowed us to test the case of an extreme rotational acceleration, as observed in the smashing mantis shrimp.

Modeling torque from drag measurements

We modeled the torque generated by drag during the strike of a raptorial appendage from our measurements of dynamically scaled models. This necessitated a consideration of the differences in flow between a rotating structure (as in mantis shrimp) and one exposed to the translating flow in a flume (as in our drag measurements). We modeled drag torque using a quasi-steady blade-element approach that treated the morphology as a series of chord-wise (i.e. in the direction of flow) elements that vary in their dimensions to conform to the shape of the dactyl–propodus unit.

The total drag generated by this structure in translating flow (F_d) was considered equal to the sum of drag on all elements, as indicated by the following equation (Batchelor, 1967):

$$F_d = \frac{1}{2}\rho \sum_{i=1}^{n} h_i (C_d)_i U^2 \Delta l, \tag{5}$$

where Δl is the thickness (i.e. linear dimension along the longitudinal axis of the structure) and h is the width (i.e. linear dimension perpendicular to flow) of each element i, with n equaling the total number of elements. This measure of drag coefficient, $(C_d)_i$, may be distinguished from the coefficient for the entire appendage, because it represents the contribution of an individual element. The drag coefficient for each element was modeled in a form similar to a uniform elliptical cylinder, given by the following equation (Hoerner, 1965):

$$C_d = k\left(1 + \frac{c}{h}\right) + 1.1\left(\frac{h}{c}\right), \tag{6}$$

where k is a shape coefficient that varies with the geometry of the structure and c is the chord length (i.e. linear dimension in the direction of flow). We measured the dimensions (c and h) from our micro-CT scans with the dactyl–propodus unit (with the dactyl closed against the propodus) for 20 evenly spaced elements. For a uniform elliptical cylinder, a fixed value for the shape coefficient (k=0.015) is predictive of empirical drag measurements (Hoerner, 1965). The shape coefficient, k, was determined for each of our dynamically scaled models from our measurements of drag using nonlinear least-squares ('lsqcurvefit' in MATLAB) to minimize deviation from our drag measurements across flow speeds.

This blade-element model of drag provided the basis for modeling the torque generated during a strike. The drag torque (τ) was modeled with the following equation (McHenry et al., 2012):

$$\tau = \frac{1}{2}\rho T_d L^5 \left(\frac{d\gamma}{dt}\right)^2, \tag{7}$$

where $d\gamma/dt$ is the angular velocity and L is length of the dactyl–propodus unit (i.e. equal to the characteristic length for Re, Eqn 4). The drag-torque index, T_d, indicates the propensity of an appendage to generate drag torque during a strike. Its calculation incorporates the variation in C_d (Eqn 6) and associated shape coefficients (k) of blade elements that we determined from drag measurements, as articulated by the following equation (McHenry et al., 2012):

$$T_d = \frac{1}{L^5}\sum_{i=1}^{n} h_i (C_d)_i r_i^3 \Delta l, \tag{8}$$

where r is the distance between an element and the pivot point of the dactyl–propodus unit, approximated as the proximal-most point on the propodus. We calculated drag torque index, T_d, across all of our measured species with the dactyl in the open and closed positions.

Effects of shape, size and kinematics on strike performance

We used our predictions of drag torque to compare strikes across morphologies and kinematics. We evaluated the maximum value of drag torque and the energetic cost of drag (E_d) which was calculated by integrating drag torque over the angular displacement of a strike (McHenry et al., 2012):

$$E_d = \int_0^{\gamma_d} \tau \, d\gamma, \tag{9}$$

where γ_d is the total angular excursion over a strike. This integral was solved numerically using the 'trapz' function in MATLAB with the strike excursion divided into 1000 equal intervals of time.

We used our model of drag torque (Eqn 7) to perform a sensitivity analysis that explored the effects of kinematics, size and shape on maximum drag-torque and drag energy. Each simulation independently modified strike duration, the length of an open or closed dactyl–propodus unit, and drag-torque index over a series of 100 simulated strikes. We varied each parameter of interest by 0.75 orders of magnitude above and below the mean value for the species while setting all other parameter values equal to the mean value for each species. For each simulation, we calculated the maximum torque (Eqn 7) and drag energy (Eqn 9).

RESULTS
Strike kinematics

Coronis scolopendra's strikes followed a sequence typical of spearer species (Table 2): (1) the dactyl opened from the propodus, (2) the propodus slid along the merus, (3) the propodus rotated

toward the prey and (4) the dactyl and propodus made contact with the prey. The slide of the propodus prior to propodus rotation indicated that the strikes were powered by spring-loaded skeletal elements. Prey distance from the mantis shrimp's eye was on average 7.12 mm (range±1 s.d.=3.68–9.94±1.96 mm). The distal tip of the propodus reached an average peak linear speed of 2.1 m s^{-1} (0.7–3.6±0.6 m s^{-1}) and average peak linear acceleration of 2600 m s^{-2} (300–11,000±1200 m s^{-2}). Peak linear velocity was reached from 0.2 to 6.1 ms after the propodus began rotating, and strike duration ranged from 2.3 to 13.1 ms.

Coronis scolopendra size and kinematics were not correlated when analyzed in terms of propodus length and maximum linear velocity (linear regression: R^2=0.07, N=6, $F_{1,5}$=0.377, P=0.57). A non-significant trend was present in the analysis of propodus length and maximum linear acceleration (linear regression: R^2=0.57, N=6, $F_{1,5}$=6.74, P=0.05).

The phylogenetic (PGLS) regression analyses of *C. scolopendra* and five previously studied species revealed a significant negative association between angular kinematics and striking body length (Fig. 5, Table 1) (angular velocity: P=0.02, R^2=0.76; angular acceleration: P=0.02, R^2=0.77). Linear kinematics were not significantly associated with size, although linear acceleration appeared to follow a non-significant negative relationship with size (P=0.06, R^2=0.6).

Computational fluid dynamics

We performed CFD simulations to test the accuracy of a blade-element model in estimating the drag on a rotating structure at the scale of a raptorial appendage. The simulation of steady, linear flow of 20 m s^{-1} on the multi-frustum model of the appendage of *G. smithii* showed considerable span-wise flow at the leading edge directed towards the free ends (frustum segments 1 to 3, and 17 to 19; numbered from proximal to distal), coupled with lower calculated drag coefficients at these outer regions compared with literature values for infinitely long elliptical cylinders (Fig. 6A). Span-wise flow at the leading edge in the proximal direction towards the mid-region of the appendage model was observed on the proximal side of the bulging part of the appendage (frustum segments 11 to 15). Drag coefficients for long elliptical cylinder from Eqn 5 for k=0.015 consistently overestimated the values calculated by the CFD simulation (frustum segments 10 to 12), but the difference was most prominent for the above-mentioned frustum segments where span-wise flow was observed (Fig. 6A). According to this CFD simulation, total drag force would be overestimated by 55% when using drag coefficients from long elliptical cylinders in a blade-element model.

The simulation of accelerated rotation of the multi-frustum model revealed a zone of high positive pressure that functioned to resist rotation at the leading edge of the elliptical cylinder. This was accompanied by a zone of high negative pressure on the proximal and lateral surfaces of the multi-frustum model (Fig. 6B,C). The performance of a blade-element model (Van Wassenbergh et al., 2008) in approximating the torque about the fixed center of rotation, as calculated by CFD, depended on the C_d input treatment (Fig. 6D–F). The model using the C_d value of a long elliptical cylinder (Eqn 5) (Hoerner, 1965) showed the largest difference: a steeper increase in the resistive torque with increasing angular velocity owing to drag forces caused this blade-element model to overestimate the final torque (at time 0.700 ms) by 54% (Fig. 6D). The difference between the two other models and the CFD solution was much smaller: the effect of drag was underestimated at the final simulation time by 4.6% in the model that used C_d values calculated

Table 2. Strike kinematics of the medium-sized spearer, *Coronis scolopendra*

No. strikes (no. prey distance measurements)	Maximum linear speed (m s^{-1})	Maximum linear acceleration (10^3 m s^{-2})	Maximum angular velocity (10^2 rad s^{-1})	Maximum angular acceleration (10^5 rad s^{-2})	Prey distance (10^{-3} m)	Time to maximum linear speed (10^{-3} s)
8 (7)	2.85±0.45 (2.19–3.56)	3.9±1.4 (2.3–6.1)	5.91±0.90 (4.58–6.90)	8.17±3.30 (4.81–14.10)	6.44±1.36 (5.03–8.64)	1.63±0.74 (0.20–2.80)
8 (7)	1.96±0.37 (1.52–2.54)	4.5±3.3 (1.7–10.5)	3.49±0.65 (2.62–4.43)	7.90±5.68 (2.86–18.20)	6.24±1.16 (5.01–8.31)	1.46±0.42 (0.80–2.13)
7 (6)	2.19±0.68 (1.23–2.89)	1.9±1.4 (0.5–4.5)	2.44±0.80 (1.34–3.26)	2.10±1.71 (0.58–5.55)	8.23±3.21 (3.90–12.80)	3.76±1.28 (2.10–5.70)
5 (4)	1.94±0.40 (1.39–2.34)	2.6±1.3 (1.1–3.7)	2.25±0.47 (1.57–2.74)	3.03±1.51 (1.24–4.24)	8.01±1.97 (5.33–10.00)	3.30±1.90 (1.20–6.10)
5 (5)	1.78±0.73 (1.15–2.83)	2.5±3.5 (0.3–8.7)	2.12±0.85 (1.36–3.31)	2.96±4.03 (0.37–10.10)	7.31±2.37 (4.33–9.19)	1.90±1.60 (0.40–4.00)
10 (9)	2.73±0.39 (1.84–3.14)	1.9±0.6 (0.8–2.6)	3.19±0.45 (2.14–3.66)	2.25±0.75 (0.88–3.03)	9.94±2.59 (4.74–12.90)	3.38±0.32 (2.90–4.00)
7 (6)	1.01±0.22 (0.74–1.41)	0.9±0.3 (0.3–1.4)	1.30±0.29 (0.93–1.82)	1.11±0.46 (0.36–1.90)	3.68±0.56 (3.00–4.68)	3.76±1.23 (1.90–5.40)

Data are presented as means±s.d. (range) for each of the seven individuals. The first individual listed was female, and the rest were males.
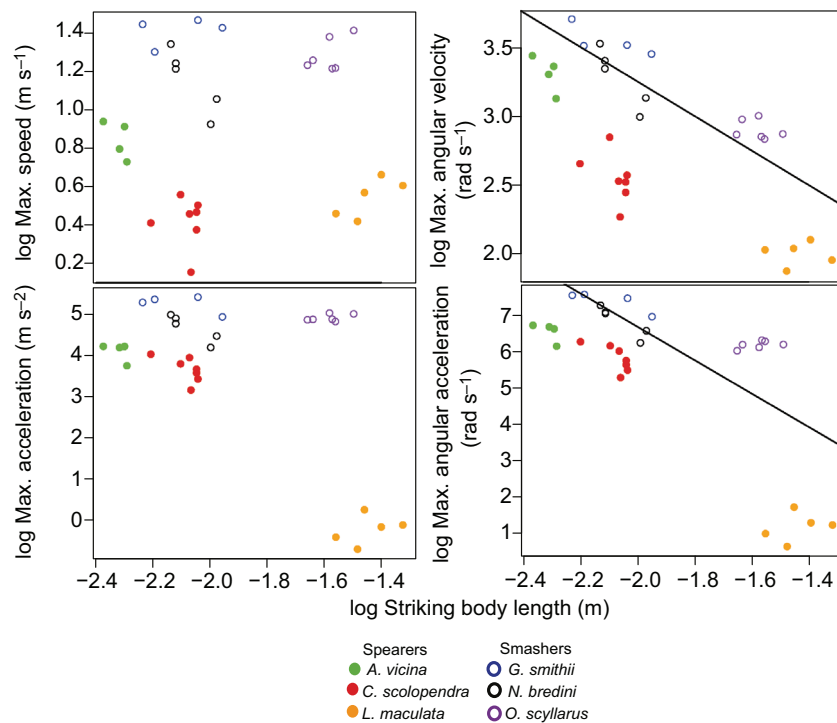
Fig. 5. Using kinematic data across six stomatopod species, the striking body length (the distance from the dactyl–propodus joint to the attachment point of the lateral extensor muscle onto the carpus; Fig. 3) exhibited a significant negative relationship with angular velocity and acceleration. Each data point represents the maximum value from each individual within each species. The overlaid regression lines were calculated using phylogenetic generalized least squares based on mean values for each species and the phylogenetic relationships of these taxa.

by the steady-flow CFD simulation (Fig. 6E), whereas the model with the C_d values from Hoerner (1965; Eqn 5 with $k=0$) decreased by 24% (to conform with the total drag force calculated by steady-flow CFD) and overestimated the resistive torque by 3.4% (Fig. 6F). In contrast, local torques along the length of the appendage yielded large differences between CFD for all three versions of the blade-element model (Fig. 6G–I). Nevertheless, a blade-element model of drag informed by a quantification of the total drag force in linear flow (Fig. 6F) offers an excellent approximation of the hydrodynamic resistance encountered by a rotating structure at the scale of a raptorial appendage. Such a model provided the basis of our calculations of the drag-torque index and the maximum torque and drag energy (see below).

Drag measurements
Our drag measurements from dynamically scaled models allowed us to consider the hydrodynamics of different appendage shapes (Table S2). The two smasher taxa (*G. smithii* and *G. falcatus*) and the undifferentiated taxon (*H. californiensis*) exhibited higher drag when the dactyl was in the open position, while the drag on spearer appendages (*C. scolopendra* and *L. maculata*) was similar regardless of whether the dactyl was opened or closed against the propodus (Table S2, Figs 3, 5).

Our blade-element model succeeded in characterizing these drag measurements. The blade-element model calculated drag from measurements of the dimensions of the appendage (Eqn 5) and by fitting a value for the shape factor, k, included in the calculation of drag coefficient (Eqn 6). For each physical model, the blade-element model succeeded in characterizing the variation in drag with respect to flow velocity to generate a high coefficient of determination ($r^2 > 0.97$; Fig. 7). The smasher species, *G. smithii* and *G. falcatus*, with a closed dactyl, exhibited variation in drag with speed similar to that predicted for a uniform elliptical cylinder with the same mean dimensions. This result emerged in spite of the fact that these species exhibited shape factors ($k \approx 0.10$, Table S3) that were more than sevenfold greater than an elliptical cylinder

($k=0.015$). This discrepancy is explained by the substantial variation in cross-sectional shape along the length of a raptorial appendage. Conversely, the raptorial appendage of *C. scolopendra* was relatively uniform along its length (Fig. 3) and, consequently, was found to possess a shape factor ($k=0.0153$) that was similar to that of an elliptical cylinder.

Effects of shape, size and kinematics on costs of movement
The drag-torque index provides a metric for the effects of the shape on the hydrodynamics of a raptorial appendage in rotation. Among the five species considered, we found that the two spearers had lower T_d than smashers and the undifferentiated *H. californiensis*. The spearers exhibited T_d values that were similar to that of a uniform elliptical cylinder (Table S3). This was because the spearers possessed a relatively uniform cross-sectional shape along the length of the appendage (Fig. 3). In contrast, the enlarged dactyl of a smasher at the distal end of the appendage yielded a relatively large value for the drag-torque index (Eqn 8). Opening the dactyl serves to move a portion of the appendage toward the distal end of the appendage, where drag generates a greater torque than when the dactyl is closed. As a consequence, the values of T_d in all species were greater with the dactyl opened than when it was closed.

We tested the individual effects of strike duration, dactyl length and drag-torque index over a series of 100 simulated strikes for three taxa (*G. smithii*, *L. maculata* and *C. scolopendra*) (Fig. 8). These simulations revealed that the maximum torque and drag energy were most sensitive to the size of the appendage and far less sensitive to strike duration and drag-torque index (Fig. 8).

DISCUSSION
Drag generated by the strike of a mantis shrimp is dominated by size and velocity and less so by shape. Larger mantis shrimp, regardless of appendage type, move more slowly, which indicates the presence of trade-offs between angular kinematics and size during the diversification of mantis shrimp raptorial appendages. In spite of their distinct morphologies, differences in the shapes of the smasher
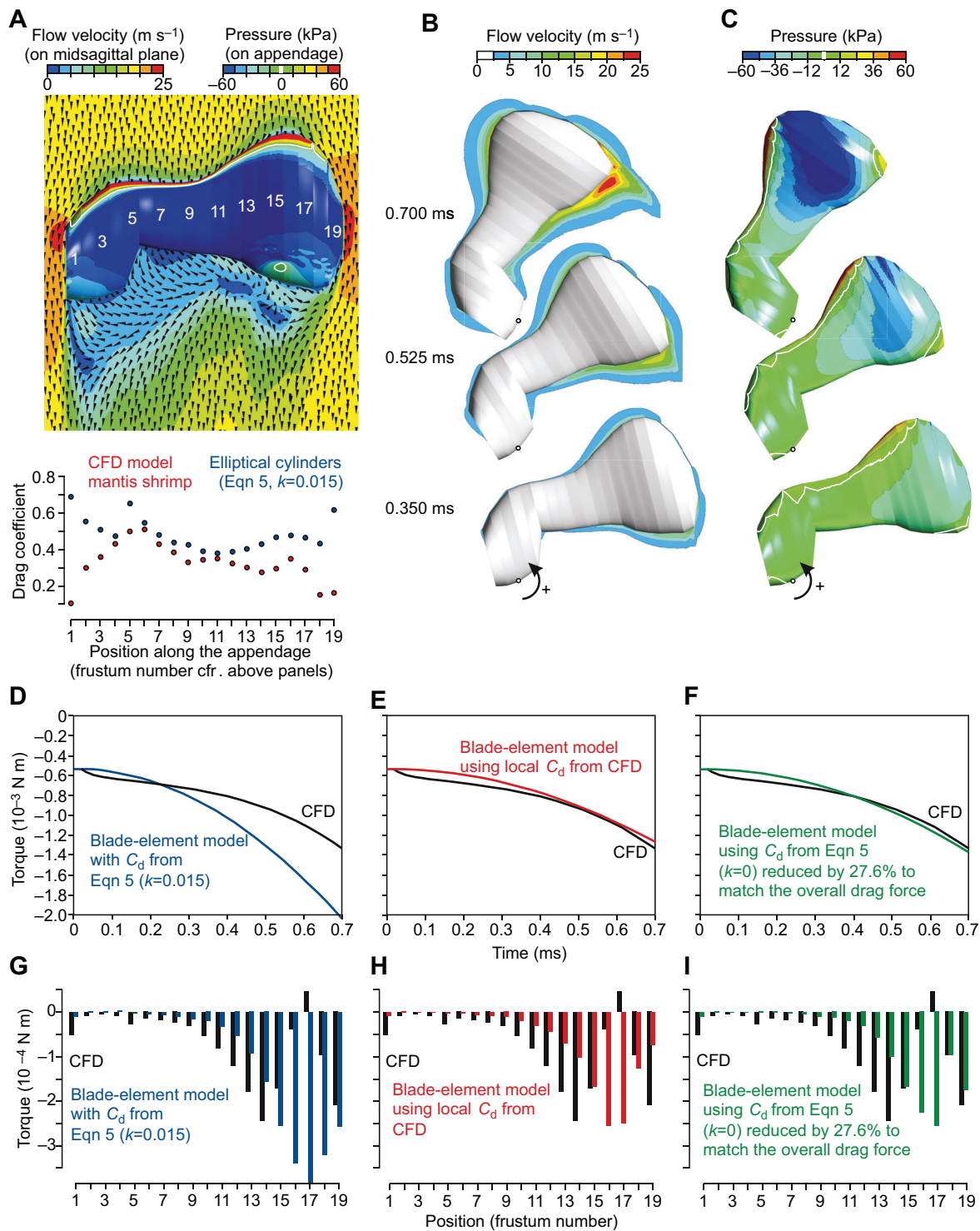
Fig. 6. Computational fluid dynamics (CFD) analyses simulated the hydrodynamics along a multi-frustum model matched to the dimensions of a mantis shrimp (see Fig. S2). (A) Patterns of steady, linear flow (20 m s⁻¹ from top to bottom) along a midsagittal plane and the associated pressure on the appendage surfaces are shown in the top panel, and a comparison of drag coefficients calculated on the separate frustum segments (red circles) with those from the literature for long elliptical cylinders of the corresponding aspect ratio (blue circles) are shown in the bottom panel. The black arrowheads show the 3D flow direction. (B) Flow velocity from the simulation of constant rotational acceleration is shown along the medial rotational plane. (C) Pressure on the surface of the rotating multi-frustum model. Velocities and pressures are shown for three instants (simulation times shown on the left of B). (D–F) The resistive torque about the joint from the water exerted on the elliptical cylinder as calculated by CFD (black curve) was compared with the torque calculated analytically using the blade-element model from Van Wassenbergh et al. (2008). Three variations of this model are shown: (D) the original model that uses drag coefficients for long elliptical cylinders (see Eqn 5); (E) a model that uses the local (i.e. per individual frustum segment) drag coefficients calculated by the steady-flow CFD simulation shown in A; and (F) a model that combines the information of the overall drag force on the appendage in steady, linear flow (from the CFD simulation shown in A) with the local aspect-ratio dependence from Eqn 5. (G–I) Local resistive torques at the final simulation time (0.700 ms) are compared between CFD (black bars) and the blade-element models (colored bars). The definition for the sign of the torque in D–I is indicated at the bottom of the contour plots (B,C).
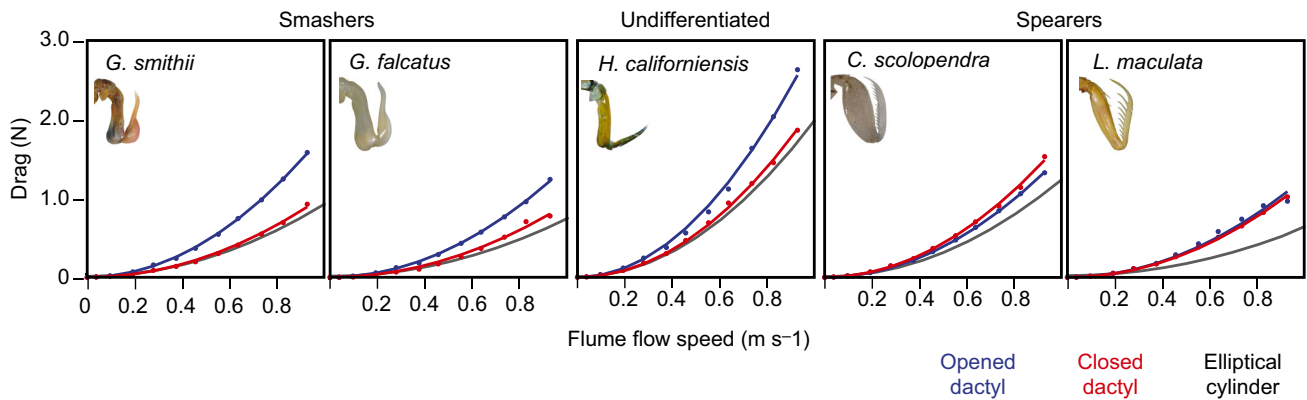
Fig. 7. To compare the empirical and analytical results, drag at varying flow speeds was determined from three sources: empirical flume measurements, drag equations with coefficients set to match appendage shape and orientation, and drag calculations using a simple shape. Drag relative to flow speed was measured in the flume using scale models in open and closed dactyl positions (blue and red circles, respectively). The calculated drag was fit to the flume data using linear least-squares regression (solid lines overlaying circles). The open-dactyl configuration yielded higher drag than the closed-dactyl orientation in all species except for the spearers, which exhibited minimal drag differences in the open and closed dactyl configurations. Using the same drag calculations, but with a drag coefficient for cylinders with elliptical (gray lines) cross-sections, the elliptical cylinders provided a lower bound to the flume-based drag measurements.

and spearer appendages did not greatly alter drag. Nonetheless, we found that smashers reduced drag by closing the dactyl, and that spearers, even with very substantial dactyls, did not experience a large change in drag with the dactyl open.

A blade-element approach adequately approximated drag when compared with the more computationally intensive CFD approach. However, there were anomalies between the two approaches that warrant further investigation when considering more detailed, future analyses of energetic costs of raptorial strikes. In particular, the interaction between shape and span-wise flow suggests that shape may be important for local flow specific to rotational movement. Nonetheless, the reasonable correspondence between blade-element and CFD models is good news for coarse-grained future comparative analyses that are, from this point forward, more feasible than if CFD were required.

Strike kinematics
The kinematic data from a medium-sized spearer, *C. scolopendra*, filled a key size range for the comparison of kinematics across stomatopod appendage types (Fig. 5, Table 1). Following the broad pattern across mantis shrimp, *C. scolopendra* struck with slightly slower kinematics than the smaller spearer *A. vicina*, and more slowly than the comparably sized smashers *G. smithii* and *N. bredini*. *Coronis scolopendra* used their spring and latch system, as indicated by the characteristic sliding and sudden outward rotation of the propodus and dactyl (Cox et al., 2014; deVries et al., 2012; Kagaya and Patek, 2016; Patek et al., 2004, 2007). Across species, angular kinematics decreased with increasing appendage size. Smashers exhibited faster kinematics for a given appendage size than non-smashers.

Modeling approaches to the hydrodynamics of fast rotations
The simplified approach of a blade-element analysis adequately approximated hydrodynamic drag when compared with a computational fluid dynamic model. Our CFD model indicated regional variation in flow, pressure and hydrodynamic torque that was not predicted by the blade-element model (Fig. 6), which treats regions along the length of the structure as independently operating sources of drag. Despite these discrepancies, as long as the shape-dependent coefficients of drag used as input in the blade-element

models do not overestimate drag in the case of steady linear flow, the blade-element model will also perform well to predict drag-torque for extremely fast rotations (Fig. 6E,F).

A previous study on the rotating head of a pipefish came to the same conclusion (Van Wassenbergh and Aerts, 2008), and our study now demonstrates that this approach is also valid for the more than 15-times higher angular velocities and more than 20-times higher angular accelerations of the fastest appendage strikes of mantis shrimp. A noteworthy discrepancy in the mantis shrimp modeling was that the pattern of local variation in the hydrodynamic torque along the length of the appendage was poorly predicted by the current blade-element models compared with the pipefish models (Fig. 6G–I versus fig. 9 in Van Wassenbergh and Aerts, 2008). Even the blade-element model of the mantis shrimp appendage that accounted for span-wise flow near the proximal and distal ends (under linear flow conditions) using locally reduced C_d values during the torque calculations still showed considerable local torque differences when compared with CFD (Fig. 6H). We assume this is caused by a different, yet related, simplification of blade-element models, namely the simplified treatment of local angles of attack.

Given that the current blade-element models treat the elements as elliptical cylinders, all surfaces in contact with the water are assumed to be parallel with the long axis. This is not the case in the more realistic CFD model that used frustum segments instead of elliptical cylinders. Therefore, the multi-frustum model appropriately accounted for variation in the angle of attack of the leading edge of the mantis shrimp appendage during rotation (Fig. 6C): the leading-edge surfaces at the distal end (frustum segments 16–18; Fig. 6A) move nearly parallel with respect to the surrounding water during rotation, whereas the more proximal leading-edge surfaces (frustum segments 10–15; Fig. 6A) move nearly perpendicularly to the water. This is reflected in the pressure patterns on the surfaces: no positive pressures are exerted by the water on the distal part of the leading edge, whereas a large zone of positive pressure is located on the more proximal part of the leading edge.

Consequently, the larger discrepancy in local torques in the mantis shrimp model (Fig. 6A) compared with the pipefish is probably due to the larger variation in the angles of attack at the
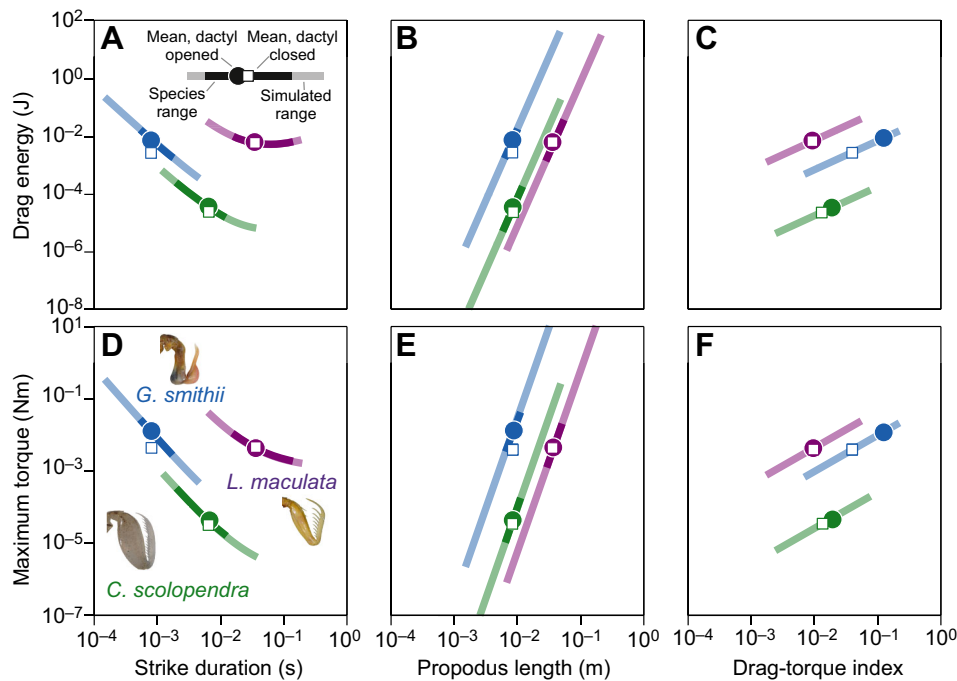
Fig. 8. Sensitivity analysis of strike duration, propodus length and the drag-torque index. Drag energy (A–C) and maximum torque (D–F) were variably sensitive to real and simulated shifts in strike duration, propodus length and drag-torque index across species (blue: smasher *G. smithii*; green: spearer *C. scolopendra*; purple: spearer *L. maculata*). Both metrics were extremely sensitive to size (B,E), such that small shifts in propodus length yielded many orders of magnitude of change in torque and drag energy that affected the three appendage types similarly. Compared with these strong effects of size, drag-torque index followed less-overlapping and less-steep increments in drag energy and torque across shifts in drag-torque index. *Lysiosquillina maculata* experienced a relatively smaller shift in drag energy across similar strike duration ranges than experienced by the other two species. The greater effect of the dactyl opening in smashers is visible via the offset between the dactyl open simulation (open square) and the closed simulation (solid circle). Note that higher strike duration indicates a slower strike (i.e. lower velocity and acceleration) and that the appendage photographs are not to scale.

distal part of the rotating structure. This effect will also be less prominent in the spearer mantis shrimp, because of their lower variation in chord lengths along their appendages (Fig. 3). Despite these local torque discrepancies, the overall congruence between the total torque output from CFD and blade-element modeling is significant for future comparative studies because it demonstrates that hydrodynamic effects that are inherent to rotational flow do not substantially impact the overall drag-torque over a wide range of angular velocities and accelerations.

Both CFD and blade-element approaches present limitations on how we have modeled drag. These techniques do not account for the effects of a transition to turbulent flow in the boundary layer of the structure. This transition, which for smooth surfaces in steady flow occurs at a *Re* of approximately 200,000, would cause drag coefficients to decrease significantly (Hoerner, 1965). However, this critical *Re* was exceeded by one species (*G. smithii*) and only for a brief period upon attaining maximum speed at the distal tip of the appendage (Table 1). A turbulent transition even in this case appears unlikely. The flow over the appendage is predominantly chord-wise, which suggests that the chord is the appropriate characteristic length for the *Re* that is predictive of the turbulent transition, which would likely yield a *Re* value below 200,000.

Our models additionally neglect surface roughness, which may induce a turbulent transition in steady flow at *Re*>20,000 (Hoerner, 1965). However, flows are far from steady during the strike of mantis shrimp. Studies on flow accelerated from rest in pipes show that the transition to a turbulent boundary layer is delayed and thereby causes the transition to occur at significantly higher *Re* (Lefebvre and White, 1989). Comparing the wake of our accelerated

simulations with steady flow simulations from CFD support the notion that the flow corresponds to the patterns of a lower *Re* (Fig. S2). Unfortunately, the combined effect of surface roughness (decreasing critical *Re*) and acceleration from rest (increasing critical *Re*) on the transition to a turbulent boundary layer is unknown. Because accelerations are extremely high, and the appendage surfaces relatively smooth, we have assumed that the boundary layer remains laminar for mantis shrimp strikes.

The suite of approaches taken in this study, including our drag measurements, blade-element analyses of shape-variant mantis shrimp appendages, and CFD analyses of rotating multi-frustum models, lends strong support to a simplified approach going forward. Furthermore, the similar excursions of strikes across taxa (Fig. S1) allow an additional level of comparative analysis that incorporates a similar kinematic profile and thus reduces the need for time-intensive kinematic analyses. Future comparative studies could therefore be performed based primarily on morphology and thereby build on and integrate the substantial understanding of morphological and mechanical evolution of this system (Anderson et al., 2014; Anderson and Patek, 2015; Blanco and Patek, 2014; Claverie et al., 2011; Claverie and Patek, 2013; Patek et al., 2007, 2013; Rosario and Patek, 2015).

The evolution of the raptorial appendage
Shape variation did not play a major role in drag, which suggests that the notable differences in smashing and spearing appendages can be largely attributed to their divergence in predatory function and morphological robustness for impaling and crushing prey (Anderson et al., 2014, 2016b; Claverie et al., 2011; Claverie and

Patek, 2013; deVries et al., 2012). In only one dimension did shape play a notable role: regardless of whether the dactyl was open or closed, the spearers had lower torque resulting from drag (T_d) than smashers. In contrast, the smashers experienced greater drag energy and drag torque with an open dactyl than with the dactyl closed in a hammering position.

The combined effects of size and speed on drag generation were substantial across mantis shrimp. A spearing mantis shrimp's strike encounters drag energy and torque comparable to that of a smashing mantis shrimp that is an order of magnitude smaller (Fig. 8B,C). If one considers drag as a proxy for energetic costs, then an upper limit on energy costs may explain the apparent evolutionary limits on maximal body size in smashers (Blanco and Patek, 2014; Patek, 2015). In other words, to move extremely fast, smasher appendages must be small. The energetic costs may be even more stringent than evidenced in the present paper, which allowed mathematical models of larger appendages to rotate more quickly; a previous hydrodynamic analysis demonstrated that higher displacement strikes intuitively associated with greater speeds (given the longer out-lever of the appendage) actually move more slowly than expected, because of the energetic costs of moving through water (McHenry et al., 2012). Future comparative analyses that more fully account for energetic costs may pinpoint more subtle variation within and across species that balances the trade-offs among these key variables.

Conclusions

Unlike the hydrodynamics of locomotor systems that must balance propulsion with drag reduction, the diversification of feeding structures operate under a different constellation of factors, such as fracture resistance, effective prey capture morphology and the reduction of feeding costs (Anderson et al., 2016a; Anker et al., 2006; Full et al., 1989; Vermeij, 1987; Weaver et al., 2012). This study demonstrates that the shapes of fast, centimeter-scale predatory structures can diversify with relatively minimal costs within the steep constraints of size and kinematics in the generation of drag.

Supplementary information
Supplementary information available online at http://jeb.biologists.org/lookup/doi/10.1242/jeb.140590.supplemental

References
Anderson, P. S. L. and Patek, S. N. (2015). Mechanical sensitivity reveals evolutionary dynamics of mechanical systems. *Proc. R. Soc. B Biol. Sci.* **282**, 20143088.
Anderson, P. S. L., Claverie, T. and Patek, S. N. (2014). Levers and linkages: mechanical trade-offs in a power-amplified system. *Evolution* **68**, 1919-1933.
Anderson, P. S. L., LaCosse, J. and Pankow, M. (2016a). Point of impact: the effect of size and speed on puncture mechanics. *Interface Focus* **6**, 20150111.
Anderson, P. S. L., Smith, D. C. and Patek, S. N. (2016b). Competing influences on morphological modularity in biomechanical systems: a case study in mantis shrimp. *Evol. Dev.* **18**, 171-181.
Anker, A., Ahyong, S. T., Noël, P. Y. and Palmer, A. R. (2006). Morphological phylogeny of alpheid shrimps: parallel preadaptation and the origin of a key morphological innovation, the snapping claw. *Evolution* **60**, 2507-2528.
Batchelor, G. K. (1967). *An Introduction to Fluid Dynamics*. Cambridge, MA: Cambridge University Press.
Blake, R. W. (1979). The mechanics of labriform locomotion I. Labriform locomotion in the Angelfish (*Pterophyllum eimekei*): an analysis of the power stroke. *J. Exp. Biol.* **82**, 255-271.
Blanco, M. M. and Patek, S. N. (2014). Muscle trade-offs in a power-amplified prey capture system. *Evolution* **68**, 1399-1414.
Caldwell, R. L. and Dingle, H. (1976). Stomatopods. *Sci. Am.* **234**, 81-89.
Claverie, T. and Patek, S. N. (2013). Modularity and rates of evolutionary change in a power-amplified prey capture system. *Evolution* **67**, 3191-3207.
Claverie, T., Chan, E. and Patek, S. N. (2011). Modularity and scaling in fast movements: power amplification in mantis shrimp. *Evolution* **65**, 443-461.
Cox, S. M., Schmidt, D., Modarres-Sadeghi, Y. and Patek, S. N. (2014). A physical model of the extreme mantis shrimp strike: kinematics and cavitation of Ninjabot. *Bioinspir. Biomim.* **9**, 016014.
deVries, M. S., Murphy, E. A. K. and Patek, S. N. (2012). Strike mechanics of an ambush predator: the spearing mantis shrimp. *J. Exp. Biol.* **215**, 4374-4384.
Dickinson, M. H., Lehmann, F.-O. and Sane, S. P. (1999). Wing rotation and the aerodynamic basis of insect flight. *Science* **284**, 1954-1960.
Fish, F. E. (1984). Mechanics, power output and efficiency of the swimming muskrat (*Ondatra zibethicus*). *J. Exp. Biol.* **110**, 183-201.
Full, R. J., Caldwell, R. L. and Chow, S. W. (1989). Smashing energetics: prey selection and feeding efficiency of the stomatopod, *Gonodactylus bredini*. *Ethology* **81**, 134-147.
Goyens, J., Van Wassenbergh, S., Dirckx, J. and Aerts, P. (2015). Cost of flight and the evolution of stag beetle weaponry. *J. R. Soc. Interface* **12**, 20150222.
Hoerner, S. F. (1965). *Fluid-Dynamic Drag*. Brick Town, NJ: self-published.
Jiang, H. and Kiørboe, T. (2011). Propulsion efficiency and imposed flow fields of a copepod jump. *J. Exp. Biol.* **214**, 476-486.
Johansson, L. C. and Lauder, G. V. (2004). Hydrodynamics of surface swimming in leopard frogs (Rana pipiens). *J. Exp. Biol.* **207**, 3945-3958.
Kagaya, K. and Patek, S. N. (2016). Feed-forward motor control of ultrafast, ballistic movements. *J. Exp. Biol.* **219**, 319-333.
Koehl, M. A. R. (1996). When does morphology matter? *Annu. Rev. Ecol. Syst.* **27**, 501-542.
Lefebvre, P. J. and White, F. M. (1989). Experiments on transition to turbulence in a constant-acceleration pipe flow. *J. Fluids Eng.* **111**, 428-432.
Lentink, D., Dickson, W. B., van Leeuwen, J. L. and Dickinson, M. H. (2009). Leading-edge vortices elevate lift of autorotating plant seeds. *Science* **324**, 1438-1440.
Li, G., Müller, U. K., van Leeuwen, J. L. and Liu, H. (2012). Body dynamics and hydrodynamics of swimming fish larvae: a computational study. *J. Exp. Biol.* **215**, 4015-4033.
Liu, H., Wassersug, R. and Kawachi, K. (1996). A computational fluid dynamics study of tadpole swimming. *J. Exp. Biol.* **199**, 1245-1260.
McHenry, M. J., Azizi, E. and Strother, J. A. (2003). The hydrodynamics of locomotion at intermediate Reynolds numbers: undulatory swimming in ascidian larvae (*Botrylloides* sp.). *J. Exp. Biol.* **206**, 327-343.
McHenry, M. J., Claverie, T., Rosario, M. V. and Patek, S. N. (2012). Gearing for speed slows the predatory strike of a mantis shrimp. *J. Exp. Biol.* **215**, 1231-1245.
Menter, F. R. (1994). Two-equation eddy-viscosity turbulence models for engineering applications. *AIAA J.* **32**, 1598-1605.
Nakata, T., Liu, H. and Bomphrey, R. J. (2015). A CFD-informed quasi-steady model of flapping-wing aerodynamics. *J. Fluid Mech.* **783**, 323-343.
Ngo, V. and McHenry, M. J. (2014). The hydrodynamics of swimming at intermediate Reynolds numbers in the water boatman (Corixidae). *J. Exp. Biol.* **217**, 2740-2751.

Patek, S. N. (2015). The most powerful movements in biology. *Am. Sci.* **103**, 330.

Patek, S. N. and Caldwell, R. L. (2005). Extreme impact and cavitation forces of a biological hammer: strike forces of the peacock mantis shrimp *Odontodactylus scyllarus*. *J. Exp. Biol.* **208**, 3655-3664.

Patek, S. N., Korff, W. L. and Caldwell, R. L. (2004). Deadly strike mechanism of a mantis shrimp. *Nature* **428**, 819-820.

Patek, S. N., Nowroozi, B. N., Baio, J. E., Caldwell, R. L. and Summers, A. P. (2007). Linkage mechanics and power amplification of the mantis shrimp's strike. *J. Exp. Biol.* **210**, 3677-3688.

Patek, S. N., Rosario, M. V. and Taylor, J. R. A. (2013). Comparative spring mechanics in mantis shrimp. *J. Exp. Biol.* **216**, 1317-1329.

Porter, M. L., Zhang, Y., Desai, S., Caldwell, R. L. and Cronin, T. W. (2010). Evolution of anatomical and physiological specialization in the compound eyes of stomatopod crustaceans. *J. Exp. Biol.* **213**, 3473-3486.

Richards, C. T. (2010). Kinematics and hydrodynamics analysis of swimming anurans reveals striking inter-specific differences in the mechanism for producing thrust. *J. Exp. Biol.* **213**, 621-634.

Rosario, M. V. and Patek, S. N. (2015). Multilevel analysis of elastic morphology: the mantis shrimp's spring. *J. Morphol.* **276**, 1123-1135.

Tanaka, Y. and Hisada, M. (1980). The hydraulic mechanism of the predatory strike in dragonfly larvae. *J. Exp. Biol.* **88**, 1-19.

Van Wassenbergh, S. and Aerts, P. (2008). Rapid pivot feeding in pipefish: flow effects on prey and evaluation of simple dynamic modelling via computational fluid dynamics. *J. R. Soc. Interface* **5**, 1291-1301.

Van Wassenbergh, S., Strother, J. A., Flammang, B. E., Ferry-Graham, L. A. and Aerts, P. (2008). Extremely fast prey capture in pipefish is powered by elastic recoil. *J. R. Soc. Interface* **5**, 285-296.

Van Wassenbergh, S., Day, S. W., Hernández, P. L., Higham, T. E. and Skorczewski, T. (2015a). Suction power output and the inertial cost of rotating the neurocranium to generate suction in fish. *J. Theor. Biol.* **372**, 159-167.

Van Wassenbergh, S., van Manen, K., Marcroft, T. A., Alfaro, M. E. and Stamhuis, E. J. (2015b). Boxfish swimming paradox resolved: forces by the flow of water around the body promote manoeuvrability. *J. R. Soc. Interface* **12**, 20141146.

Vermeij, G. J. (1987). *Evolution and Escalation: An Ecological History of Life*, p. 527. Princeton, NJ: Princeton University Press.

Versluis, M., Schmitz, B., von der Heydt, A. and Lohse, D. (2000). How snapping shrimp snap: through cavitating bubbles. *Science* **289**, 2114-2117.

Walker, J. A. (2002). Rotational lift: something different or more of the same? *J. Exp. Biol.* **205**, 3783-3792.

Walker, J. A. (2004). Dynamics of pectoral fin rowing in a fish with an extreme rowing stroke: the threespine stickleback (*Gasterosteus aculeatus*). *J. Exp. Biol.* **207**, 1925-1939.

Weaver, J. C., Milliron, G. W., Miserez, A., Evans-Lutterodt, K., Herrera, S., Gallana, I., Mershon, W. J., Swanson, B., Zavattieri, P., DiMasi, E. et al. (2012). The stomatopod dactyl club: a formidable damage-tolerant biological hammer. *Science* **336**, 1275-1280.

Webb, P. W. and Blake, R. W. (1985). Swimming. In *Functional Vertebrate Morphology* (ed. M. Hildebrand, D. M. Bramble, K. F. Liem and D. B. Wake), pp. 120-128. Cambridge, MA: Belknap Press.
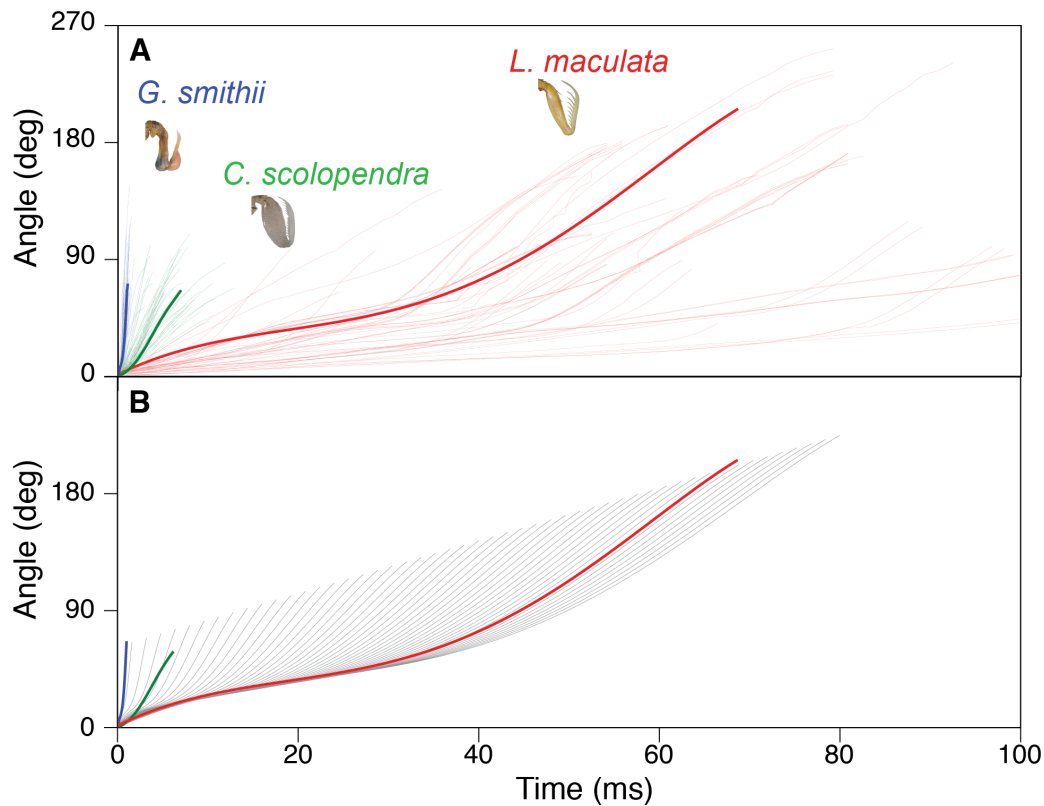
Supplementary Figures

Figure S1. Similar strike kinematics across mantis shrimp permitted generalized strike simulations. (A) Using kinematic data from previous studies and the present study, propodus rotations during raptorial strikes were plotted over time [red: *Lysiosquillina maculata* (deVries, et al. 2012); green: *Coronis scolopendra* (this study); blue: *Gonodactylus smithii* (Cox, et al. 2014)] and the strike that was closest to the mean strike duration for the species was determined for each species (bolded lines). (B) We simulated the kinematics of all species with a fifth-order polynomial for the sigmoidal pattern of one particular strike from *L. maculata*. A sequence of strike simulations is shown (gray curves) that have scaled this strike to varying strike durations to illustrate how this simulated motion compares to the average strikes of each species (i.e., the same strike highlighted in A).
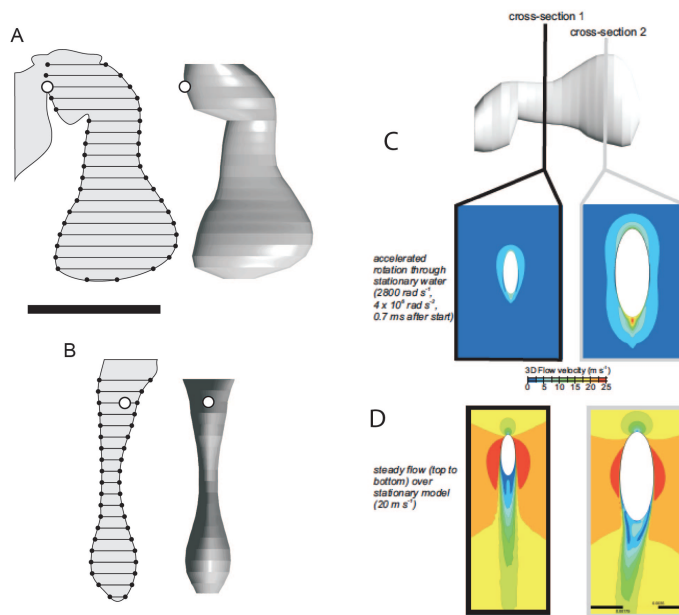
Figure S2. Computational fluid dynamic models and flow patterns in accelerated and steady flow over the model. A. Dimensions of the multi-frustum model fitted to the striking appendage of *Gonodactylus smithii* used in the computational fluid dynamics model. The open circle indicates the center of rotation, and corresponds to the joint location between the carpus and merus (McHenry et al. 2012). The line drawings show the appendage contours (based on Figure 4 from McHenry et al. 2012) together with the axes of the twenty elliptical cylinders that served as base and top planes of the series of frustum segments (final 3D object views on the right). Lateral view images (distal to the toward right of page, dorsal toward the top of the page). **B.** Distal-proximal view images with lateral to the right, dorsal toward the top of the page. Note that the model assumes mirror symmetry about the sagittal plane through the long axis of the appendage. Scale bar, 5 mm. **Flow-patterns in the case of accelerated rotation of the mantis shrimp model (C), and for steady linear flow over the same model (D) as calculated by CFD**. The results for 3D flow velocities are shown on two cross-sectional planes (position indicated in the top image). Note that the perspective differs between the two simulations: the model is moving through stationary water in (C), while the water is moved past the stationary model in (D). This figure shows that the flow pattern in the wake of a short acceleration from rest is notably different from the fully developed wake in a steady translation where two-sided vorticity patterns are present.
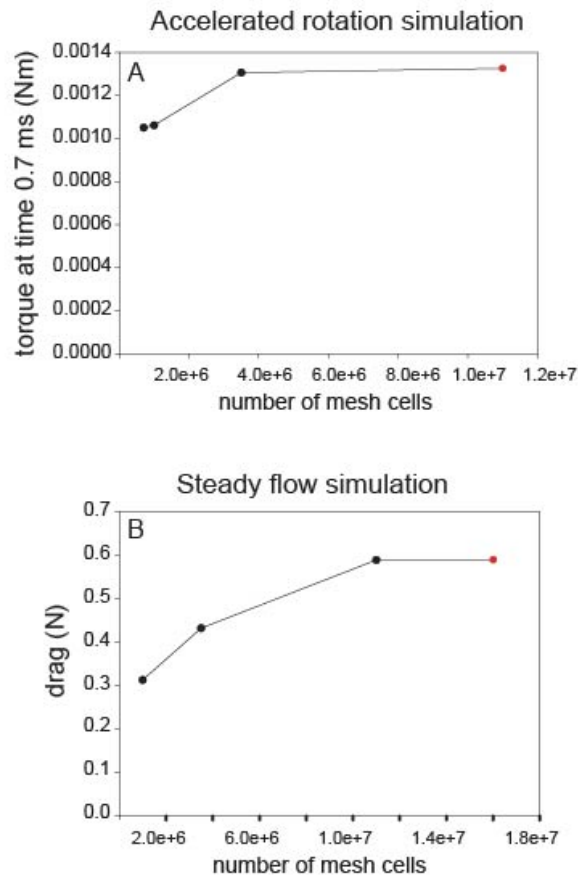
Figure S3. **Results from the mesh convergence analysis showing that the final mesh (red sphere) reached a converged solution for torque on the mantis shrimp model in the simulation of accelerated rotation (A) and for the steady flow simulation of linear flow over the model (B).**

Supplementary Tables

Table S1. Scaling of physical models to achieve the same Reynolds number as calculated for the maximum speed and propodus length of each species (Table 1).

	Maximum speed (m/s)	Propodus length (m)	Scaled appendage (m)	Scale factor	Reynolds Number
G. smithii	30	0.005	0.15	30	1.4×10^5
G. falcatus	30	0.005	0.15	30	1.4×10^5
H. californiensis	3	0.027	0.24	9	7.7×10^4
C. scolopendra	3.4	0.0085	0.23	30	2.7×10^4
L. maculata	3	0.058	0.23	4	1.7×10^5

The scale factors were used for setting the range of flume speeds (Table 3). Given that the maximum flow velocity of the flume is 1 m/s, the scale factor is equivalent to the maximum modeled speed for each scaled-up appendage. *G. falcatus* models were run at speeds based on published values for *G. smithii* (Cox, et al. 2014). *H. californiensis* models were run at speeds based on published values from *L. maculata* (deVries, et al. 2012).

Table S2: Drag (N) on each physical model tested

Flume speed (m/s)		0.038	0.096	0.19	0.28	0.38	0.46	0.55	0.64	0.74	0.83	0.93
	Drag (N)											
G. smithii	open	<0.01	0.02	0.07	0.16	0.24	0.37	0.54	0.74	0.98	1.25	1.58
	closed	<0.01	0.01	0.04	0.09	0.13	0.20	0.30	0.41	0.55	0.69	0.93
G. falcatus	open	<0.01	0.02	0.06	0.12	0.18	0.29	0.43	0.57	0.76	0.96	1.24
	closed	<0.01	<0.01	0.03	0.07	0.10	0.17	0.26	0.36	0.51	0.70	0.78
H. californiensis	open	<0.01	0.03	0.12	0.24	0.38	0.56	0.83	1.12	1.63	2.04	2.63
	closed	<0.01	0.03	0.09	0.18	0.30	0.47	0.69	0.94	1.19	1.45	1.86
C. scolopendra	open	<0.01	0.02	0.06	0.14	0.21	0.33	0.47	0.63	0.84	1.06	1.33
	closed	<0.01	0.02	0.07	0.15	0.24	0.37	0.53	0.70	0.91	1.14	1.53
L. maculata	open	<0.01	0.02	0.05	0.11	0.18	0.29	0.42	0.58	0.74	0.91	0.97
	closed	<0.01	0.02	0.05	0.11	0.17	0.26	0.39	0.51	0.65	0.82	1.02

Each model was tested at a range of flume speeds with the dactyl in the open or closed position. Drag on each model configuration and flume speed is shown here.

Table S3. Hydrodynamic metrics of shape, determined from drag measurements

Species	k		T_d		
	Dactyl closed	Dactyl open	Dactyl closed	Dactyl open	Cylinder
G. smithii (Smasher)	1.06×10^{-1}	5.39×10^{-2}	3.79×10^{-2}	12.0×10^{-2}	8.40×10^{-2}
G. falcatus (Smasher)	1.08×10^{-1}	5.13×10^{-2}	2.08×10^{-2}	3.38×10^{-2}	2.69×10^{-2}
H. californiensis (Undifferentiated)	3.75×10^{-2}	3.08×10^{-2}	1.95×10^{-2}	5.00×10^{-2}	4.87×10^{-2}
C. scolopendra (Spearer)	1.53×10^{-2}	3.95×10^{-2}	1.32×10^{-2}	1.77×10^{-2}	1.62×10^{-2}
L. maculata (Spearer)	3.80×10^{-2}	5.82×10^{-2}	0.95×10^{-2}	0.96×10^{-2}	1.05×10^{-2}

k, shape coefficient; T_d, drag-torque index